Programmable 4D Printing of Photoactive Shape Memory Composite Structures

Yongdie Deng, Fenghua Zhang,* Menglu Jiang, Yanju Liu, Huiping Yuan, and Jinsong Leng*

Cite This: *ACS Appl. Mater. Interfaces* 2022, 14, 42568−42577

Read Online

ACCESS | 📊 Metrics & More | 📖 Article Recommendations | 🔲 Supporting Information

ABSTRACT: 4D printing is an advanced manufacturing technology combining additive manufacturing with smart materials. Based on light-active shape memory composites, smart medical structures with remote control capability, therapeutic function, and biocompatibility are hopefully fabricated by 4D printing. Here, a multifunctional composite with good mechanical properties, biocompatibility, and light-active shape memory performance is prepared by incorporating gold nanoparticles into a shape memory polyurethane matrix. The composites demonstrate a rapid and stable light-thermal effect, which can achieve localized and controlled breast tumor ablation, providing an approach to hyperthermia treatment for cancer cells. By directly bioprinting the composite melt, a series of 4D-printed structures are manufactured accurately in a convenient, clean, and safe way, which show a fast autonomous light-driven shape recovery process. The examples of a 4D-printed soft tissue scaffold and intraluminal scaffold can expand from a conveniently insertional shape to an expanded shape under light exposure. The proposed strategies provide great inspiration for customized multifunctional light-thermal therapeutic structures for minimally invasive treatment.

KEYWORDS: 4D printing, shape memory composites, light-active, light-thermal therapy, smart structure
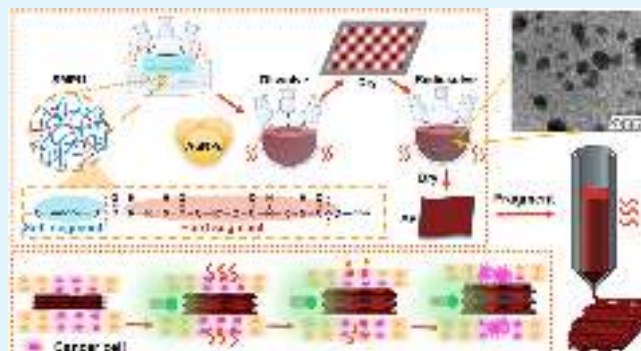
1. INTRODUCTION

Shape memory polymers (SMPs) are a class of smart polymers that can spontaneously transform from a temporary shape to a permanent shape under external stimuli,[1] including heat,[2,3] light,[4,5] solutions,[6] electrical fields,[7,8] and magnetic fields.[9,10] SMPs have been widely used in many fields, such as aerospace,[11] biomedical applications,[12,13] and optoelectronic fields.[14,15] Currently, heat-driven SMPs, achieving shape recovery by directly heating above their transition temperatures (T_{trans}), have been widely investigated. Among them, shape memory polyurethane (SMPU) has a molecular microphase structure, including soft segments and hard segments. The T_{trans} of SMPU is determined by the melting point of the soft segment and the permanent shape is determined by the hard segment.[16] The polyester SMPU is promising in the biomedical field because of the adjustable T_{trans}, good mechanical properties, and biocompatibility.[17] Light-active SMPs have attracted increasing attention because light can provide contactless spatial and temporal control.[18,19] So far, most light-active SMPs are achieved by introducing light-responsive molecular switches or adding fillers with light-thermal effects. Commonly used fillers are organic dyes,[20−22] carbon nanomaterials,[23,24] rare earth organic complexes,[25] and metal nanoparticles such as gold nanoparticles (AuNPs).[26]

AuNPs have good biocompatibility and can reduce toxicity to the kidney.[27]

In decades, several printed methods have been successfully developed, such as direct writing (DW),[28] fused deposition modeling (FDM),[29] selected laser sintering (SLS),[30] and stereolithography (SLA).[31,32] 3D printing of SMPs endows structures with smart performance, which is also called 4D printing.[33−35] 4D printing has been one of the most advanced techniques for prospective applications in the biomedical field.[36,37] Among them, contactless remote control structures have received more attention, such as magnetic-active[10] and light-active 4D-printed structures.[38] However, magnetic drive often requires a huge magnetic coil to provide a magnetic field, and it is difficult to give specific local stimulation. Then, the construction of structures by FDM requires a printed filament, which is a relatively tedious process. The SLA technology has strict requirements on the photocuring performance of
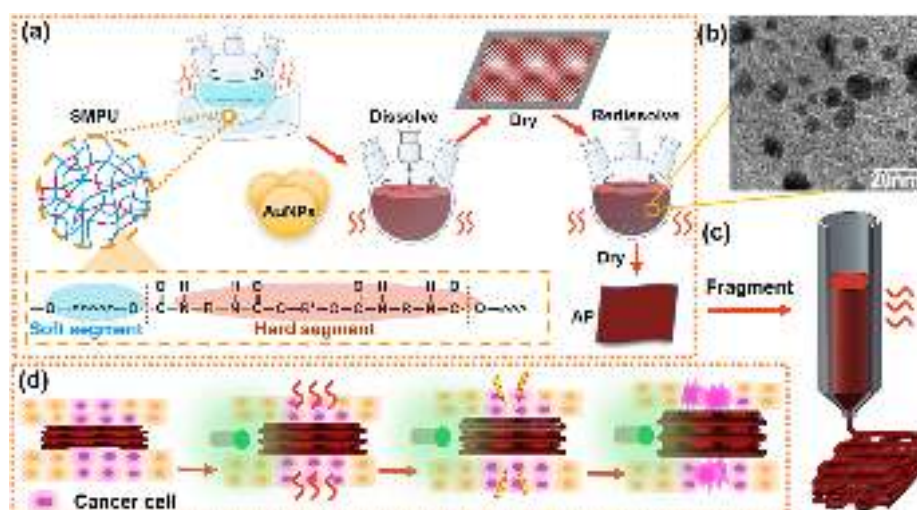
Figure 1. (a) Schematic diagram of preparing the AP composite. (b) TEM image of the AP mixture. (c) Printing process of the AP composite melt by the DW technique. (d) Schematic diagram of a 4D-printed medical structure allowing for facilitated deployment by light-active shape recovery while possessing a therapeutic effect.

materials, and it is still doubtful whether an initiator can be safely applied to implanting materials in the biomedical field.

Here, a series of AuNPs/PU (AP) composites with a light-active shape memory effect were prepared by adding AuNPs into the SMPU matrix through secondary dissolution (Figure 1a,b). A variety of tests were used for researching the thermal, mechanical, and shape memory properties of the AP composites. Under light irradiation with different intensities, the light-thermal effects of AP composites were tested, and the hyperthermia treatment of cancer cells by light-thermal performance was carried out in vitro. By directly bioprinting the composite melt, a series of 4D-printed structures are manufactured accurately in a convenient, clean, and safe way (Figure 1c), which showed a fast autonomous light-driven shape recovery process. The examples of a 4D-printed soft tissue scaffold and intraluminal scaffold can expand from a facilitated insertion to an expansion shape under the light stimulus. The addition of AuNPs not only endowed these 4D-printed structures with controllable autonomous shape recovery properties but also provided an approach for hyperthermia therapy (Figure 1d). This work opens a new route for the development of customized multifunctional photothermal therapeutic structures through the synergistic combination of light-active shape memory composites and 4D printing.

2. EXPERIMENTAL SECTION

2.1. Preparation of SMPU. Hexamethyldiisocyanate (HDI), N-dimethylformamide (DMF), dibutyltin dilaurate (DBTDL), and 1,4-butanediol (BDO) were purchased from Aladdin Reagent (Shanghai) Co., Ltd., China. Polycaprolactone diol (PCL-OH) was purchased from Hunan Juren Chemical Hitechnology Co., Ltd., China. First, 10 g of PCL-OH with a molecular weight of 2000 was added into a three-mouth flask and vacuumized for 3 h at 120 °C. Then, 2.6 g of HDI was diluted by 20 g of DMF and added into the flask. DBTDL (0.5 g) as a catalyst was added for a 3 h reaction at 90 °C in a nitrogen atmosphere. The reaction was then cooled to 70 °C. Afterward, 0.9 g of BDO was diluted by 30 g of DMF and added into the mixture for a 2 h reaction. Finally, the mixture was poured into a mold to obtain the SMPU films by drying at 60 °C.

2.2. Preparation of AuNPs/PU Composites. As shown in Figure 1a, three groups of SMPU films weighing 2 g were respectively dissolved in 30 g of DMF at 70 °C and labeled as groups 1, 2, and 3.

Then, 2, 4, and 6 g of AuNP colloids (0.1 wt %, Xuzhou Jiechuang New Materials Technology Co., Ltd., China) were added drop by drop into groups 1, 2, and 3, respectively. Then, the three groups of the mixture were dried for 6 h at 100 °C to obtain a wine-red powder. Afterward, the three groups of powder were respectively dissolved in DMF at 70 °C, stirred for 2 h, and then ultrasonic-oscillated for 2 h to get the homogeneous AP mixture. As the transmission electron microscopy (TEM) image shows (Figure 1b), the AuNPs did not agglomerate or coagulate during the mixing process. Comparatively, the AuNPs in the mixed solution after the second dissolution are more evenly distributed than those after the first dissolution (Figure S1). Finally, the AP1, AP2, and AP3 films were obtained by drying these mixtures.

2.3. Characterization. The UV−vis absorption spectra of AuNP colloids and AP mixtures were measured by a UV spectroradiometer (UV7, Mettler Toledo, Switzerland) at a wavelength of 200−800 nm. Attenuated total reflection Fourier transform infrared spectroscopy (ATR-FTIR, PerkinElmer Corporation, USA) was used for testing the chemical bonds and functional groups. The spectral range was 4000−650 cm^{-1}, and the resolution was 4 cm^{-1}. The crystallography of samples was analyzed by an X-ray diffractometer (X'PERT, PANalytical Corporation, Netherlands). The samples were smooth films with a dimension of 20 × 20 × 0.5 mm. Test conditions were set as a Cu target, a scanning speed of 5°/min, and a 2θ angle range of 10−80°. The endothermic curves of samples at 0−200 °C were measured by differential scanning calorimetry (DSC, DSC1, Mettler Toledo, Switzerland). The samples were weighed 6−10 mg, and the heating rate was 5 °C/min. Thermogravimetric analysis (TGA, TGA/DSC1, Mettler Toledo, Switzerland) was used to research the mass loss curves of samples in a flowing nitrogen atmosphere. The initial mass of the samples was 10−15 mg, and the heating rate was 8 °C/min. The tensile properties were tested on a universal tester (Zwick/Roell Z010, Zwick GmbH & Co. KG) with a prestress of 0.01 MPa and a tensile rate of 5 mm/min. All the tensile samples were cut into dumbbell-shaped films according to ASTM D638, Type IV. The extending creep and relaxation experiments were conducted on a dynamic thermomechanical analyzer (Q800, TA Instruments, USA). All the samples had a dimension of 50 × 5 × 0.5 mm. The preload was 0.001 N.

The rheological properties of AP melts were tested with a rotary rheometer (DHR2, TRIOS Company, Germany). The samples have a diameter of 25 mm and a height of 1 mm. The parallel plates with a diameter of 25 mm and a fixture gap of 800 nm were chosen for the tests. For the degradation experiment in vitro, the PU and AP membranes with a dimension of 20 mm × 10 mm × 0.5 mm were weighed and then put into Erlenmeyer flasks filled with Hanks'
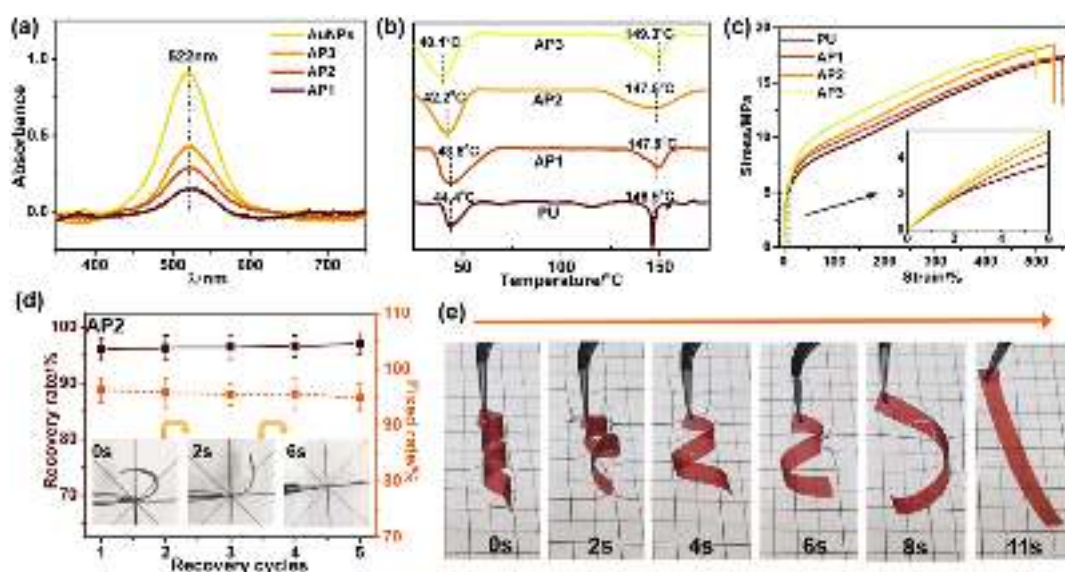
Figure 2. (a) UV−vis absorption spectra of AuNP colloid and AP1, AP2, and AP3 mixtures. (b) DSC curves of AP1, AP2, and AP3 composites. (c) Tensile stress−strain curves at 25 °C. (d) Shape recovery and fixation rates of the AP2 strip at 45 °C. (e) Shape recovery process of the AP2 strip shaped into a spiral shape at 45 °C.

solution (Fuzhou Feijing Biological Technology Co., Ltd., China). The flasks were placed into a shaker incubator at 37 °C. The samples were taken out at intervals, washed with deionized water, and vacuum-dried. The weight loss (ω_l) was calculated by

$$\omega_l = \frac{m(t) - m_0}{m_0} \times 100\%$$ (1)

where $m(t)$ is the weight of the specimen on time t after degradation, and m_0 is the original weight before degradation.

2.4. Cell Viability of Cancer Cells. Human breast cancer cells (MDA-MB-231) were chosen to research the cell viability of PU and AP samples after different treatments. Six groups were set up, including blank, PU, PU + light, AP, AP + light, and H_2O_2. For positive and negative controls, cells were cultured in a complete medium containing 100 mM hydrogen peroxide and a complete medium, respectively. AP and PU films were cut into circular sheets with a diameter of 8 mm for cell culture. MDA-MB-231 cells were cultured in Dulbecco's modified Eagle medium (DMEM) containing 10% fetal bovine serum (FBS) and 1% penicillin/streptomycin in an incubator at 5% CO_2 and 37 °C. The tests were performed in 12-well plates with a seeding density of 5×10^4 cells per well. After culturing for 24 h, AP and PU sheets were placed on a polycarbonate 12-well Transwell membrane (Corning Inc., Corning, NY, USA) and inserted above the seeded cells. Then, 100 μL of the medium was added on top of the inserts. After another 48 h of culture, the cells in AP + light and PU + light groups were exposed to light irradiation with a wavelength of 520 nm and a power density of 2 W/cm² for 2 min. In addition, human umbilical vein endothelial cells (HUVECs) were chosen to compare the light-thermal damage to cancer cells and normal human somatic cells after the same light irradiation of the AP composite. The culture and experimental procedures for HUVECs were the same as aforementioned. Then, the culture medium was removed, and the cell viability was evaluated by the CCK-8 assay. In detail, 10 μL of CCK-8 reagent was added to 90 μL of DMEM to generate a working solution, of which 100 μL was added per well and cultured for 1 h. One hundred microliters of working solution was collected from each well and added to a 96-well plate. The absorbance value at 450 nm was recorded by a microplate reader. Cell viability was calculated by:

$$\text{viability} = \frac{OD - OD_{blank}}{OD_{control} - OD_{blank}} \times 100\%$$ (2)

where OD is the absorbance at 450 nm after different treatments, $OD_{control}$ is the absorbance at 450 nm in the control group, and OD_{blank} is the absorbance at 450 nm in the medium. Moreover, living/dead staining of cells was performed with Calcein-AM and PI solutions (Calcein-AM/PI, Beyotime). After treatments, the medium was removed and the cells were washed with PBS. Afterward, the cells were incubated for 30 min with 0.3 μL of Calcein-AM and 0.3 μL of PI in DMEM without phenol red (300 μL per well). Then, the fluorescence images were observed with an inverted optical microscope (Leica, Germany). In addition, cells were collected after treatments, resuspended in 200 μL of Annexin V binding buffer, and then stained with 5 μL of Annexin V and 10 μL of PI for 15 min at room temperature. The percentage of apoptotic cells was evaluated by flow cytometry (BD FACSCanto II Flow Cytometer, BD Bioscience).

2.5. Fabrication of 4D-Printed AuNPs/PU Composite Structures. Models of 4D-printed structures were created in Solidworks software. The 4D-printed AP structures were manufactured by the high-temperature printed mode of 3D-Bioplotter (EnvisionTEC, Germany). First, the barrel was assembled with an extrusion needle with a diameter of 0.4 mm. Film specimens cut into fragments were added into the barrel and preheated at 144 °C for 10 min. The barrel temperature, extrusion pressure, and printed speed were set as 144 °C, 1.5 bar, and 10 mm/s, respectively. The shell thickness was 0.2 mm. The infill type was linear with an infill spacing of 0.2 mm.

3. RESULTS AND DISCUSSION

3.1. Properties of AuNPs/PU Composites. The average size of the AuNPs can be estimated by UV−vis spectroscopy. As Figure 2a shows, the UV−vis spectra of AuNP colloid and AP1, AP2, and AP3 mixtures all show obvious absorption peaks at 522 nm, indicating that the diameters of AuNPs are all about 10 nm. The result indicates that AuNPs did not agglomerate during the mixing process, which was consistent with the TEM image. All of the HDI had participated in the synthetic process because there is no stretching vibration absorption peak of the isocyanate group (N=C=O) near 2273 cm⁻¹ in the PU FTIR spectrum (Figure S2).[39] As DSC curves show (Figure 2b), the T_{trans} values formed from PCL crystals in the soft segment are all lower than 44 °C, indicating that the composite is friendly for biomedical application. The XRD curves can further verify the existence of crystals (Figure
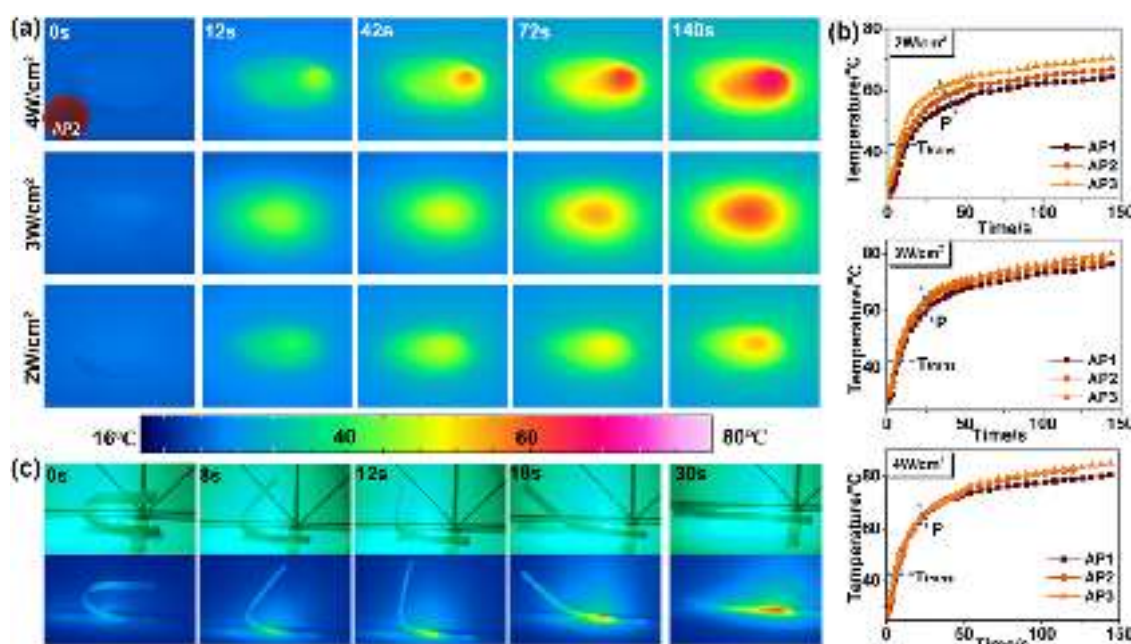
Figure 3. (a) Infrared thermal images of the AP2 film under the irradiation of 4 W/cm^2. (b) Light-thermal heating curves of AP1, AP2, and AP3 films under light with intensities of 2, 3, and 4 W/cm^2. (c) Light-active shape memory performance of AP2 strips under the light irradiation of 2 W/cm^2.

S3). The addition of AuNPs improves thermal stability. As Figure S4 shows, the remaining mass fractions of PU, AP1, AP2, and AP3 at 600 °C are 0.93, 1.05, 1.13, and 1.26%, respectively. Higher contents of AuNPs also lead to a slower degradation rate (Figure S5). In addition, AuNPs can improve strength, and the elongation at break (ε_m) of PU reaches more than 500%, showing excellent toughness (Figure 2c). Compared with PU, the ε_m of AP2 slightly decreases, while the tensile strength slightly increases, because AuNPs can entangle some molecular chain segments to hinder slippage. The creep strain of AP3 is also the smallest, indicating that AuNPs can hinder the creep process from promoting the stability of the 4D-printed structures (Figure S6).

The shape memory cycle of the AP composite can be described as follows: the sample is shaped into a temporary shape by external force upon heating above T_{trans}. The temporary shape is fixed after cooling below T_{trans} and removing the external force. Then, the sample can return to its original shape upon reheating above T_{trans}. The shape memory properties of AP strips at 45 °C are calculated in Table S1 according to Figure S7. The shape recovery and fixed rates were all above 95%. In addition, the shape recovery time was around 6 s. Taking AP2 strips as an example (Figure 2d), the shape recovery and fixed rates were still maintained above 95% after five shape memory cycles. As Figure 2e shows, the AP2 strip shaped into a spiral shape can recover from the temporary shape to a flat permanent shape within 11 s in 45 °C water, indicating that the AP composites have excellent shape memory properties.

3.2. Hyperthermia Treatment Based on the Light-Thermal Effect. Under light irradiation, the surfaces of AuNPs generate heat by the plasma resonance effect and increase the temperature of the PU matrix. AP1, AP2, and AP3 films were cut into circular sheets with a diameter of 12 mm and placed under a xenon lamp source (Solar-500, Beijing Newbit Technology Co., Ltd., China). The films were

irradiated by a beam with a wavelength of 520 nm at three kinds of intensities (2, 3, and 4 W/cm^2). The heating process was recorded with an infrared imager (JENOPTIK InfraTec, Germany). As Figure 3a shows, the temperature of the AP2 film under the irradiation of 4 W/cm^2 is significantly higher than that of the other two groups. The infrared thermal images of AP1 and AP3 films also show a similar rule (Figures S8 and S9). It was worth noting that the light source was not standard parallel light. With the light spot center as a center, circular areas with a diameter of 4 mm on the films were marked, and the average temperatures in these areas were recorded. As Figure 3b shows, the temperatures increase rapidly at the beginning and then are gradually stabilized. AP2 only takes 22 s to reach point P (Table S2) and needs 5 s to reach its T_{trans} (Table S3) at 4 W/cm^2, indicating fast light-responsiveness. By regulating the radiation duration and power density, the AP composites possessed controllable light-thermal performance. Under different light intensities, the shape memory properties are tested and calculated in Table S4. The shape recovery and fixed rates of AP1, AP2, and AP3 under three light intensity levels were all more than 90%. Taking AP2 strips at 2 W/cm^2 as an example (Figure 3c), the strip can recover to its original shape within 30 s, indicating remarkable light-active shape memory performance.

The T_{trans} of the AP composite is close to the commonly used temperature range in hyperthermia treatment for different kinds of cancer cells (Figure S10), indicating that it is possible to achieve hyperthermia while realizing shape memory recovery by the light-thermal effect. AP2 was chosen for the next research. After 48 h of coculture of the PU and AP circular sheets and breast cancer cells, these sheets were placed in close contact with cancer cells and exposed to light with a wavelength of 520 nm and an intensity of 2 W/cm^2. As shown in Figure 4a, the cell viability of PU and AP without light irradiation is similar to that in the blank group, which remains above 90%, indicating that PU and AP have excellent
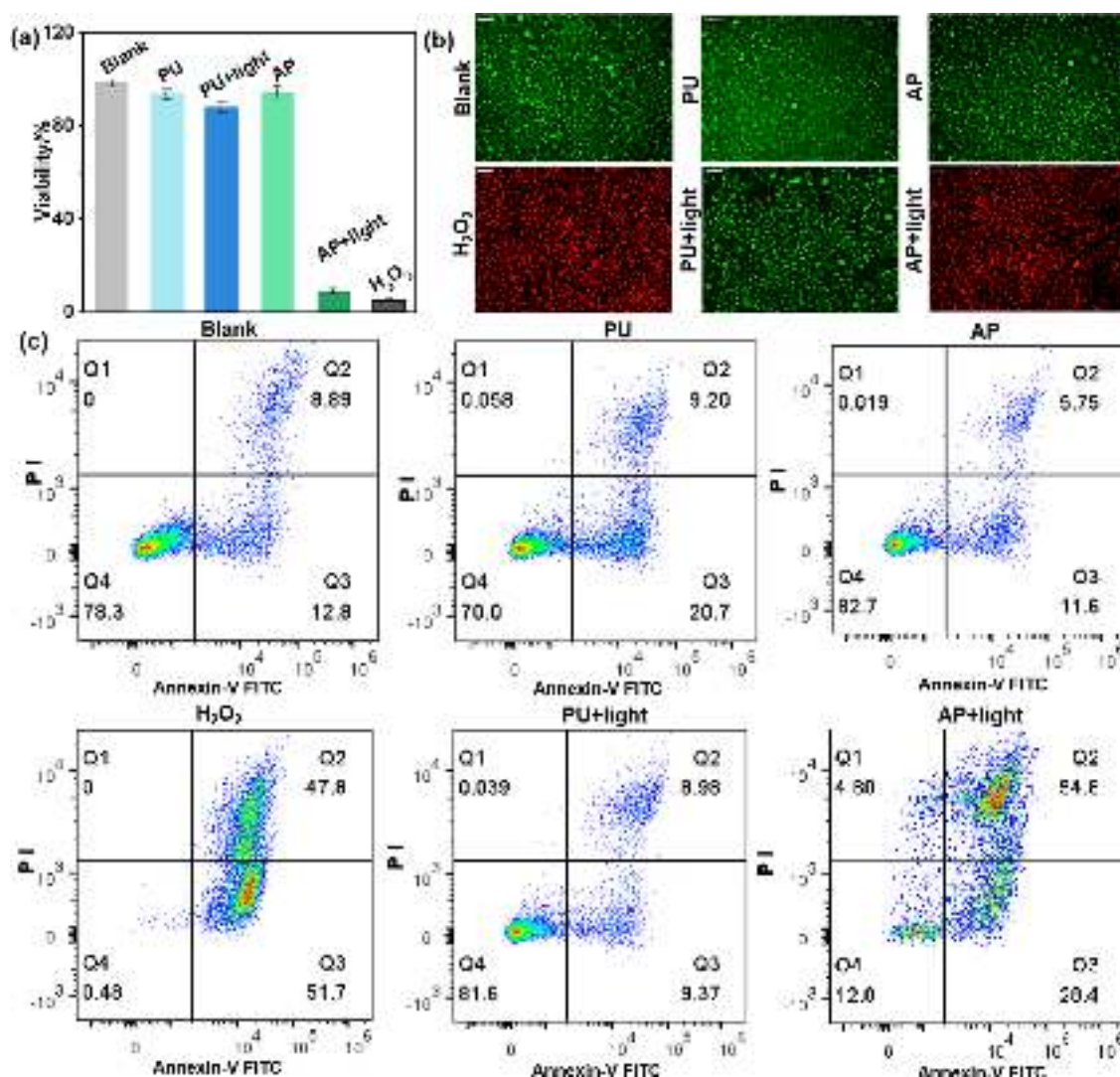
Figure 4. (a) Cell viability of cancer cells after different treatments including blank, PU, PU + light, AP, AP + light, and H_2O_2. (b) Fluorescence images of live−dead staining of breast cancer cells in different conditions. (c) Dot plots of flow cytometry analysis of samples after different treatments (lower left quadrant corresponding to live, upper right quadrant corresponding to early apoptosis, and bottom right quadrant corresponding to late apoptosis).

cytocompatibility. In addition, the cell viability of PU under light for 150 s does not have a significant decrease compared with the blank group, demonstrating that the light exposure is not cytotoxic for cancer cells. In contrast, the viability of AP under light for 150 s remarkably decreases below 10%, which is close to that in the H_2O_2 group. As shown in Figure S11, the HUVEC viability under light for 150 s is remarkably higher than the cancer cell viability, indicating that the damage to cancer cells after the same time and intensity of light irradiation is significantly greater than that to normal cells.

Then, the viability status of the cancer cells was visualized by live−dead staining. The living and dead cells were stained green and red, respectively. As Figure 4b shows, the fluorescence images of AP, PU, and blank groups are filled with living cancer cells stained green. However, the cancer cells in the AP + light group show a mass of red fluorescence from a large number of dead cells, indicating that the light-thermal effect of AP for killing cancer cells is significant. Comparatively, the AP + light (HUVECs) group has a large number of surviving HUVECs (Figure S12), visually indicating that the damage to normal human cells is less than that to cancer cells.

Controlling the light exposure time can result in a confined cancer cell death with the size of the dead zone matching the dimensions of the AP film. As Figure S13 shows, the fluorescence images after light irradiation of 120 s show the obvious dead−alive boundary matching the outline of the AP film region. Cancer cells without contact with the AP film do not die under light, demonstrating that the AP composite can efficiently achieve localized and controlled tumor ablation through light-thermal performance for hyperthermia treatment of cancer. As Figure 4c shows, about 54.8% of cancer cells die from early apoptosis and 28.4% from late apoptosis in the AP + light group after 150 s of light irradiation. Late apoptosis was identified as the dominant mechanism of cell death induced by the light-thermal effect. These results indicate that the light-thermal effect of AP is efficient for killing cancer cells and feasible for hyperthermia treatment of cancer.

3.3. Design on Printed Parameters. Through the DW technology, the printed process can be simplified while ensuring material cleanliness. Therefore, it is necessary to study the rheological properties of the AP melt to obtain appropriate printed parameters. The printed process of the AP
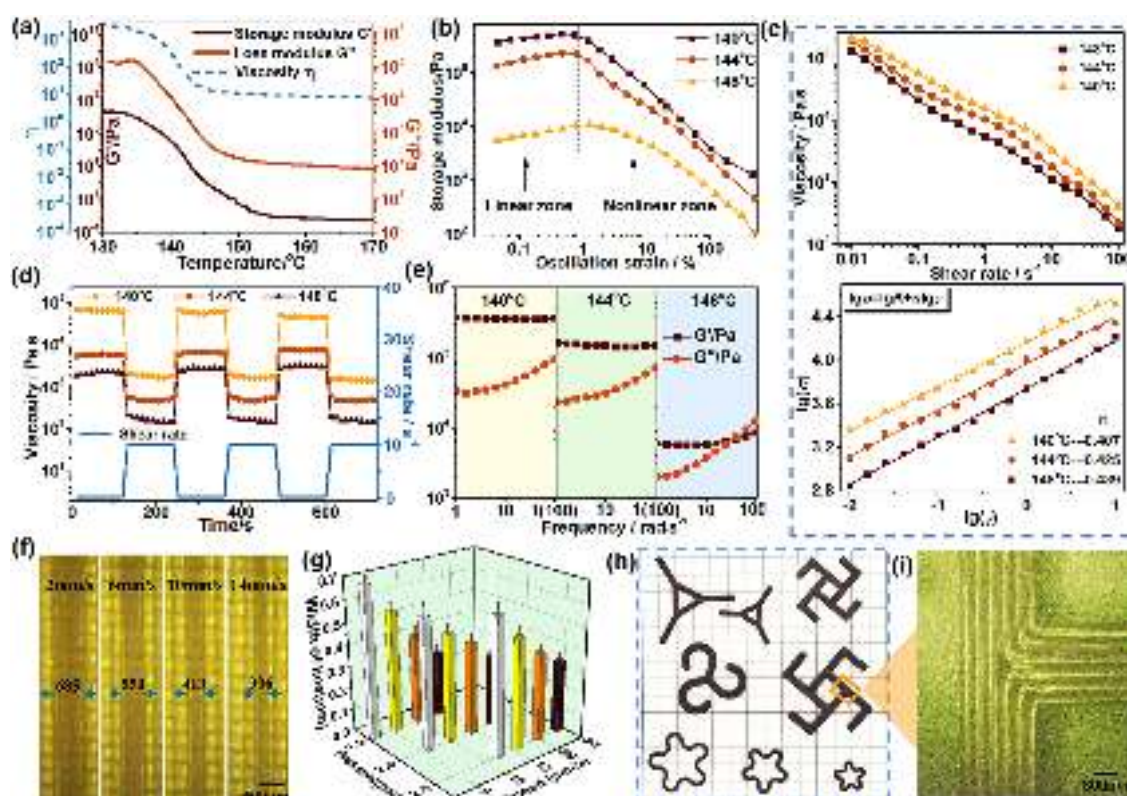
Figure 5. (a) Viscosity−temperature curve under steady state and G' and G'' curves with temperature in oscillation mode of the AP melt. (b) Curves of G' to oscillation strain at 140, 144, and 148 °C. (c) Shear viscosity−shear rate curves plotted in a logarithmic coordinate under steady state and logarithmic shear stress−shear rate curves. (d) Viscosity curves under alternating high and low shear rates. (e) Variation curves of G' and G'' with frequency. (f) Printed filaments extruded with a pressure of 1.5 bar at the printed speeds of 2, 6, 10, and 14 mm/s. (g) Line widths of printed filaments obtained at different pressures and speeds. (h) Some 4D-printed structures with various shapes. (i) Structural details under a 30× light microscope.

melt can be divided as follows: the composite was first heated into the melt in the barrel and then extruded through the nozzle under pressure. Finally, the extruded printed filaments were arranged from a preset path to form a complex 3D component.

The condition of the AP sample upon heating can be reflected through the change of storage modulus G', loss modulus G'', and viscosity η. As Figure 5a shows, the viscosity curve under steady-state mode decreases significantly between 138 and 144 °C. Under the oscillation mode, G' and G'' curves also decrease significantly between the temperature ranges. Three temperature points (140, 144, and 148 °C) corresponding to the stages of during melting, basically melting, and completely melting were selected for the following tests. As Figure 5b shows, G' curves under 140, 144, and 148 °C have a few changes in the linear zone but decrease significantly when the strain increases above the critical strain value γ_c. In the nonlinear zone, the internal structure would be damaged by the shear force.[40]

The AP melt would endure a high shear rate when extruded through a narrow nozzle, so the shear-thinning characteristic is necessary to facilitate extrusion. Figure 5c shows the steady-state shear curves of the AP melt at 140, 144, and 148 °C. All the curves decrease with the increase in shear rate, showing obvious shear-thinning characteristics. Since the measured shear stress and shear rate in logarithmic coordinates show a nearly linear relationship (Figure 5c), the power-law model can be used to express the relationship between shear rate and viscosity:

$$\eta(\dot{\gamma}) = K \cdot \dot{\gamma}^{n-1} \tag{3}$$

where K represents the parameter of the material. n is the non-Newtonian exponent. When $n > 1$, the fluid is a dilatancy fluid. When $n < 1$, the melt is a pseudoplastic fluid. n can be obtained from the Ostwald−Dewaele power rate formula:

$$\ln \sigma = \ln K + n \ln \dot{\gamma} \tag{4}$$

By linear fitting of the point of logarithmic shear stress−shear rate, the n values at 140, 144, and 148 °C can be obtained, which were 0.407, 0.425, and 0.439, respectively. The n values were all less than 1, indicating that the AP2 melt was a pseudoplastic fluid.

In the process of printing, the melt would be subjected to low shear force in the barrel, then subjected to high shear force when it passes through the nozzle, and finally subjected to low shear force after extrusion. It is necessary for the melt to have a fast response to alternating low−high−low shear force. As the thixotropy test result shows (Figure 5d), the viscosity of the AP melt decreases significantly at high shear rates and recovers rapidly at low shear rates, indicating a fast response to alternating shear rates. To further determine the printed temperature, the variation curves of G' and G'' to the frequency at 140, 144, and 148 °C were tested. The ratio of G' to G'' reflects the ratio of elasticity to viscosity in the melt. As Figure 5e shows, G' is much larger than G'' at 140 °C, indicating that the sample presents solid-like characteristics. At 148 °C, G' is less than G'' at high frequency, indicating that the melt is not conducive to the support force and shape fixation.
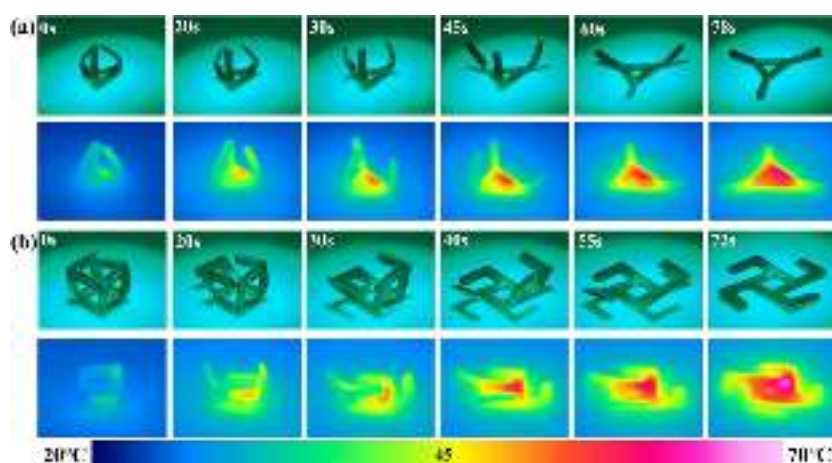
Figure 6. (a) Shape recovery process and infrared thermal images of a 4D-printed claw under light. (b) Shape recovery process and infrared thermal images of a 4D-printed hexahedral structure under light.
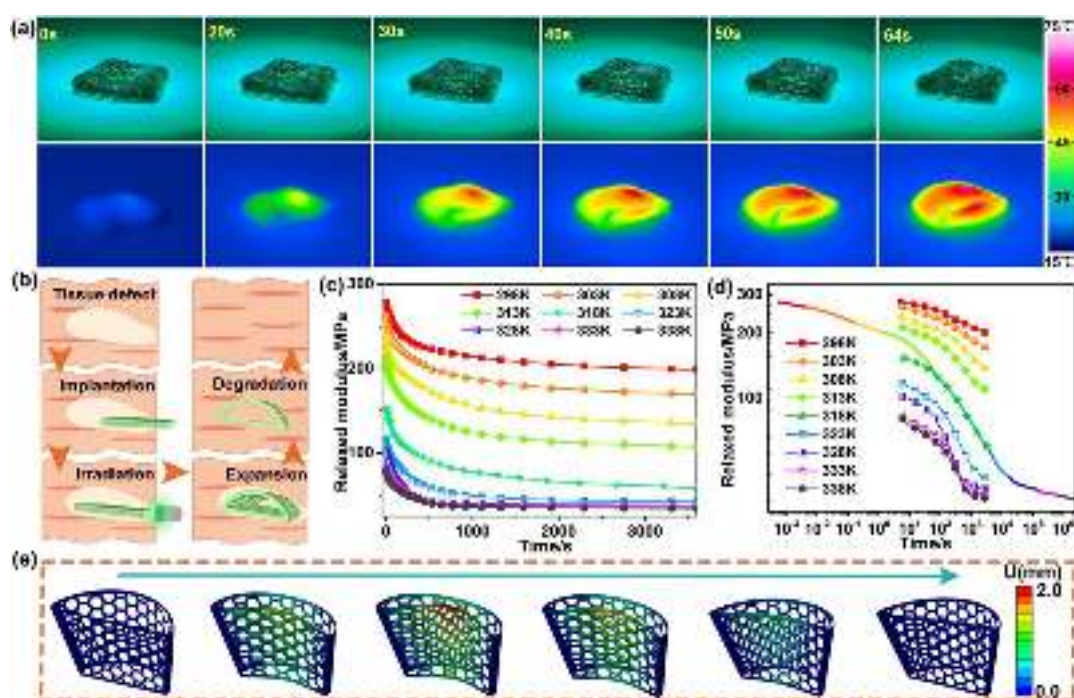

Figure 7. (a) Light-driven shape recovery process of the 4D-printed tissue scaffold and its infrared thermal images. (b) Schematic diagram of the mechanism of the tissue scaffold as a temporary medical structure for supporting tissue. (c) Stress relaxation curves of AP samples at different temperatures. (d) Stress relaxation curves in logarithmic coordinates and primary relaxation modulus curve. (e) Simulated shape recovery process of the tissue scaffold.

Thus, choosing 144 °C as the printed temperature can make the melt maintain the printed filament shape and, meanwhile, have certain fluidity.

At 144 °C, a needle with a diameter of 0.4 mm, three groups of printed pressures (1.5, 2, and 2.5 bar), and corresponding four kinds of printed speeds were chosen to study the appropriate printed parameters. Figure 5f shows the printed filaments extruded at the speed values of 2, 6, 10, and 14 mm/s under the pressure of 1.5 bar. The same method was used to obtain the printed filaments under pressures of 2 and 2.5 bar at four kinds of printed speeds (Figure S14). As Figure 5g shows, too slow printed speed would result in wider filaments compared to the diameter needle, while too fast printed speed would lead to thin filaments and some defects. The three groups of parameters closest to the needle diameter were 1.5

bar and 10 mm/s, 2 bar and 14 mm/s, and 2.5 bar and 20 mm/s. Selecting 1.5 bar and 10 mm/s as printed parameters, some 4D-printed structures were manufactured (Figure 5h). By observing the structural details under a 30× light microscope (Figure 5i), it can be seen that the printed filaments are arranged neatly and evenly at the corner, indicating that the AP melt has excellent printed capability under reasonable printed parameters.

3.4. Light-Active Shape Memory Performance of 4D-Printed Structures. For 4D-printed AP structures, the incorporated AuNPs generate heat under light to promote shape recovery, ensuring remote and selective actuation. As Figure 6a shows, a 4D-printed structure looking like a flat claw is shaped into a tightened claw, which gradually unfolds into a planar structure after 78 s under the light with a power

intensity of 2 W/cm^2. At 20 s, the claw structure has obvious shape expansion. Meanwhile, the overall temperature range is about 42 to 45 °C within the body tolerance, making it of great significance for the application of grasping objects by remote control in the biomedical field. As Figure 6b shows, the 4D-printed structure can be shaped into a hexahedron shape, like a square box, and then gradually unfolds under light within 70 s. The structure can load items and then spontaneously expand to realize the load and release of carried items by remote control. Multiple 4D-printed AP structures can quickly revert to their initial shape with contactless stimuli, showing excellent potential for remote control applications.

4D-printed smart structures based on the AP composite with good biodegradability provide inspiration for minimally invasive surgery to fill tissue defects caused by cancer lesions or build therapeutic platforms for the lumen of lesions. A tissue scaffold with a complex pore structure was constructed by 4D bioprinting of the AP melt. The tissue scaffold was compressed to a flat shape and then heated to 44 °C at 15 s under irradiation with an intensity of 2 W/cm^2. When the time reaches 70 s, the scaffold fully expands from the compressed shape to the hollow permanent shape (Figure 7a). A schematic diagram displays the mechanism of the tissue scaffold as a medical structure (Figure 7b). The tissue scaffold is compressed to a flat temporary shape and then implanted at the site of tissue injury. Then, the light source can be introduced from the wound. The scaffold can recover to its permanent shape under light stimuli to fill the defect and act as a temporary platform for cell growth because of the good biodegradability of the AP composite (Figure S15). The shape recovery process was simulated by ABAQUS Software. The thermoviscoelastic behavior of the AP composite is temperature-dependent, and a higher relaxation time is needed to achieve the same relaxation modulus at low temperature (Figure 7c). Taking 318 K as the reference temperature value (T_s), the other eight relaxation curves can be translated to obtain the primary relaxation modulus curve in logarithmic coordinates (Figure 7d). Afterward, the parameters required for the simulation can be obtained (Figures S16 and S17). As Figure 7e shows, the upper and lower surfaces of the scaffold are gradually extruded and deformed during the heating and loading step. When entering the reheating step, the temporary shape gradually returns to the initial shape. The displacement is zero at the initial moment and then returns to zero after a shape memory cycle (Figure S18). The experiment and simulation on the shape memory behaviors of the 4D-printed tissue scaffold demonstrate the feasibility of minimally invasive therapy through the shape memory property in the biomedical field.

In addition, a 4D-printed intraluminal scaffold was prepared by the AP melt. The scaffold was compressed to a flat shape and then can expand completely within 70 s in the pipeline model under the light with a power intensity of 2 W/cm^2 (Figure 8a). This allowed the fabrication of a scaffold that is easily deployed ex vivo and that expands upon light irradiation. The schematic diagram of a 4D-printed lumen scaffold for treating the lumen of lesions is shown in Figure 8b. Under the guidance and monitoring of CT, ultrasound, or magnetic resonance imaging equipment, the 4D-printed intraluminal scaffold and light source are introduced into the lesion site of the human body through natural channels or small wounds with puncture needles or catheters for minimally invasive treatment. Then, the intraluminal scaffold expands to support
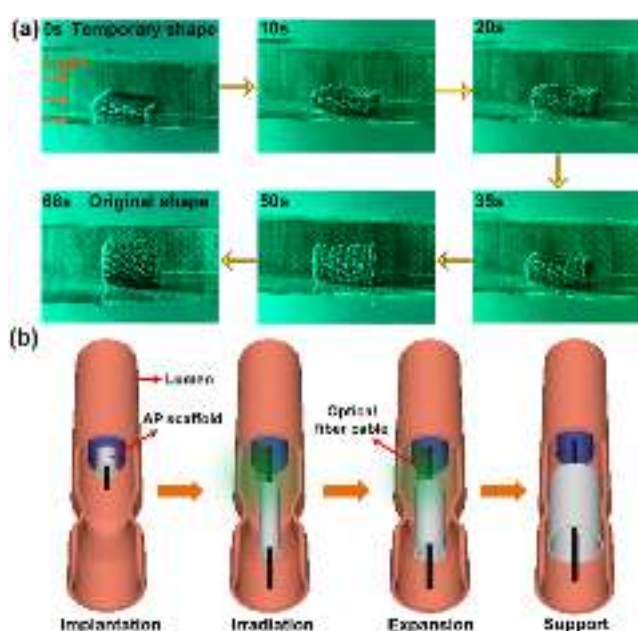

Figure 8. (a) Light-driven shape recovery process of the 4D-printed intraluminal scaffold in the pipeline model under the light in the access pipeline. (b) Schematic diagram of the mechanism of the intraluminal scaffold as a temporary medical structure for supporting a pathological lumen.

the cavity under light irradiation and simultaneously kills the cancer cells. According to the needs, the appropriate scaffold can be designed and prepared by 4D printing of the AP composite, achieving the purpose of hyperthermia, minimally invasive surgery, and personalized treatment.

4. CONCLUSIONS

In summary, 4D-printed structures were developed by direct writing of a shape memory composite melt, which showed excellent light-active shape memory performance and hyperthermia ability for biomedical application. By incorporating AuNPs into the SMPU matrix, AP composites with good biocompatibility and mechanical properties are prepared. Under the light irradiation of 4 W/cm^2, the composites with a AuNP content of 0.3 wt.% can be heated above T_{trans} within 5 s and recover the original shape within 20 s, showing fast light-thermal responsiveness and shape recovery speed. The shape fixed and recovery rates all reached more than 90%. For in vitro hyperthermia treatment of breast cancer cells, the cell viability drops 80% after light exposure for 150 s. The cancer cells without contact with the AP composite do not die, indicating that the composite can efficiently achieve localized and controlled breast tumor ablation through light-thermal performance. Subsequently, the printed parameters were obtained for direct writing bioprinting of the AP melt based on its rheological properties. A series of 4D-printed structures were manufactured and can realize the autonomous light-driven shape recovery within 80 s. The examples of a 4D-printed soft tissue scaffold and intraluminal scaffold can expand from a flat compression shape to a hollow shape without contact, showing potential for minimally invasive and personalized treatment. In conclusion, this work opens a new route for the development of customized multifunctional photothermal therapeutic structures through the synergistic

combination of light-active shape memory composites and 4D printing.

ASSOCIATED CONTENT

Ⓢ Supporting Information

The Supporting Information is available free of charge at https://pubs.acs.org/doi/10.1021/acsami.2c13982.

TEM images of the AP mixture after the first dissolution and second dissolution (Figure S1); FTIR spectrum of the PU, AP1, AP2, and AP3 composites (Figure S2); XRD curves of the PU, AP1, AP2, and AP3 composites (Figure S3); TGA curves of the PU, AP1, AP2, and AP3 composites (Figure S4); DTG curves obtained by a derivative of TGA curves (Figure S5); creep curves of the PU, AP1, AP2, and AP3 composites under stress of 2 MPa at 25 °C (Figure S6); programmed shape memory process of AP composite strips (Figure S7); infrared thermal image of the AP1 film (Figure S8); infrared thermal image of the AP3 film (Figure S9); statistical diagram of temperature range of hyperthermia treatment for different kinds of cancer cells (Figure S10); cell viability of cancer cells and HUVECs after different treatments including blank, AP, and AP + light (Figure S11); fluorescence images of live−dead staining of HUVECs in different conditions (Figure S12); fluorescence staining images after 120 s of light irradiation with an intensity of 2 W/cm^2 (Figure S13); printed filaments extruded under pressures of 2 bar and 2.5 bar (Figure S14); weight loss curves in vitro degradation experiment of AP composites (Figure S15); shape memory properties of AP composites at T_{trans} = +5 °C (Table S1); time to reach point P (Table S2); time (s) to reach the T_{trans} (Table S3); shape memory properties of AP1, AP2, and AP3 under different light intensities (Table S4); detailed derivation and calculation procedures for simulation parameters (Figures S16−S18) (PDF)

AUTHOR INFORMATION

Corresponding Authors

Fenghua Zhang − *Centre for Composite Materials and Structures, Harbin Institute of Technology (HIT), Harbin 150000, People's Republic of China*; Email: fhzhang_hit@163.com

Jinsong Leng − *Centre for Composite Materials and Structures, Harbin Institute of Technology (HIT), Harbin 150000, People's Republic of China*; ⓞ orcid.org/0000-0001-5098-9871; Email: lengjs@hit.edu.cn

Authors

Yongdie Deng − *Centre for Composite Materials and Structures, Harbin Institute of Technology (HIT), Harbin 150000, People's Republic of China*

Menglu Jiang − *Department of Ophthalmology, The Second Affiliated Hospital of Harbin Medical University, Harbin 150000, People's Republic of China*

Yanju Liu − *Department of Astronautic Science and Mechanics, Harbin Institute of Technology (HIT), Harbin 150000, People's Republic of China*

Huiping Yuan − *Department of Ophthalmology, The Second Affiliated Hospital of Harbin Medical University, Harbin 150000, People's Republic of China*; ⓞ orcid.org/0000-0001-8750-6191

Complete contact information is available at: https://pubs.acs.org/10.1021/acsami.2c13982

Notes

The authors declare no competing financial interest.

ACKNOWLEDGMENTS

REFERENCES

(1) Zheng, X.; Zhou, S.; Li, X.; Weng, J. Shape Memory Properties of Poly(d,l-lactide)/Hydroxyapatite Composites. *Biomaterials* **2006**, *27*, 4288−4295.

(2) Zhang, Y.; Zhang, N.; Hingorani, H.; Ding, N.; Wang, D.; Yuan, C.; Zhang, B.; Gu, G.; Ge, Q. Fast-Response, Stiffness-Tunable Soft Actuator by Hybrid Multimaterial 3D Printing. *Adv. Funct. Mater.* **2019**, *29*, 1806698.

(3) Liu, Y.; Zhang, W.; Zhang, F.; Lan, X.; Leng, J.; Liu, S.; Jia, X.; Cotton, C.; Sun, B.; Gu, B.; Chou, T. Shape Memory Behavior and Recovery Force of 4D printed Laminated Miura-Origami Structures Subjected to Compressive Loading. *Compos. Part B Eng.* **2018**, *153*, 233−242.

(4) Bai, X.; Yang, Q.; Li, H.; Huo, J.; Liang, J.; Hou, X.; Chen, F. Sunlight Recovering the Superhydrophobicity of a Femtosecond Laser-Structured Shape-Memory Polymer. *Langmuir* **2022**, *38*, 4645−4656.

(5) Liang, R.; Yu, J.; Wang, L.; Wang, N.; Amin, B. NIR Light-Triggered Shape Memory Polymers Based on Mussel-Inspired Iron-Catechol Complexes. *Adv. Funct. Mater.* **2021**, *31*, 2102621.

(6) Xue, J.; Ge, Y.; Liu, Z.; Liu, Z.; Jiang, J.; Li, G. Photoprogrammable Moisture-Responsive Actuation of a Shape Memory Polymer Film. *ACS Appl. Mater. Interfaces* **2022**, *14*, 10836−10843.

(7) Yu, K.; Liu, Y.; Leng, J. Conductive Shape Memory Polymer Composite Incorporated with Hybrid Fillers: Electrical, Mechanical, and Shape Memory Properties. *J. Intel. Mat. Syst. Struct.* **2011**, *22*, 369−379.

(8) Gong, X.; Xie, F.; Liu, L.; Liu, Y.; Leng, J. Electro-Active Variable-Stiffness Corrugated Structure Based on Shape-Memory Polymer Composite. *Polym.-Basel* **2020**, *12*, 387.

(9) Lin, C.; Lv, J.; Li, Y.; Zhang, F.; Li, J.; Liu, Y.; Liu, L.; Leng, J. 4D-Printed Biodegradable and Remotely Controllable Shape Memory Occlusion Devices. *Adv. Funct. Mater.* **2019**, *29*, 1906569.

(10) Zhao, W.; Zhang, F.; Leng, J.; Liu, Y. Personalized 4D printing of Bioinspired Tracheal Scaffold Concept Based on Magnetic Stimulated Shape Memory Composites. *Compos. Sci. Technol.* **2019**, *184*, No. 107866.

(11) Wang, L.; Zhang, F.; Liu, Y.; Leng, J. Photosensitive Composite Inks for Digital Light Processing Four-Dimensional Printing of Shape Memory Capture Devices. *ACS Appl. Mater. Interfaces* **2021**, *13*, 18110−18119.

(12) Montgomery, M.; Ahadian, S.; Huyer, L.; Rito, M.; Civitarese, R.; Vanderlaan, R.; Wu, J.; Reis, L.; Momen, A.; Akbari, S. Flexible

Shape-Memory Scaffold for Minimally Invasive Delivery of Functional Tissues. *Nat. Mater.* **2017**, *16*, 1038−1046.

(13) Chen, H.; Wang, L.; Zhou, S. Recent Progress in Shape Memory Polymers for Biomedical Applications. *Chin. J. Polym. Sci.* **2018**, *36*, 905−917.

(14) Zhao, L.; Zhang, L.; Zhao, J.; Shi, J.; Dai, Z.; Wang, G.; Zhang, C.; Li, B.; Feng, X.; Zhang, H.; Zhang, J.; Zhang, Z. Engineering Surface Patterns with Shape Memory Polymers: Multiple Design Dimensions for Diverse and Hierarchical Structures. *ACS Appl. Mater. Interfaces* **2019**, *11*, 1563−1570.

(15) Jin, B.; Song, H.; Jiang, R.; Song, J.; Zhao, Q. Programming a Crystalline Shape Memory Polymer Network with Thermo-and Photo-Reversible Bonds Toward a Single-Component Soft Robot. *Sci. Adv.* **2018**, *4*, No. eaao3865.

(16) Wang, Y.; Jeng, U.; Hsu, S. Biodegradable Water-Based Polyurethane Shape Memory Elastomers for Bone Tissue Engineering. *ACS Biomater. Sci. Eng.* **2018**, *4*, 1397−1406.

(17) Su, J.; Gao, W.; Trinh, K.; Kenderes, S.; Lin, J. 4D printing of Polyurethane Paint-Based Composites. *Int. J. Smart Nano Mater.* **2019**, *10*, 237−248.

(18) Lv, J.; Liu, Y.; Wei, J.; Chen, E.; Qin, L.; Yu, Y. Photocontrol of Fluid Slugs in Liquid Crystal Polymer Microactuators. *Nature* **2016**, *537*, 179−184.

(19) Qiu, Y.; Yang, Y.; Valenzuela, C.; Zhang, X.; Yang, M.; Xue, P.; Ma, J.; Liu, Z.; Wang, L.; Feng, W. Near-Infrared Light-Driven Three-Dimensional Soft Photonic Crystals Loaded with Upconversion Nanoparticles. *Adv. Opt. Mater.* **2022**, *10*, 2102475.

(20) Chen, Y.; Yu, H.; Quan, M.; Zhang, L.; Yang, H.; Lu, Y. Photothermal Effect of Azopyridine Compounds and Their Applications. *RSC Adv.* **2015**, *5*, 4675−4680.

(21) Zhou, L.; Liu, Q.; Lv, X.; Gao, L.; Fang, S.; Yu, H. Photoinduced Triple Shape Memory Polyurethane Enabled by Doping with Azobenzene and GO. *J. Mater. Chem. C* **2016**, *4*, 9993−9997.

(22) Obiweluozor, F.; Ghavaminejad, A.; Maharjan, B.; Kim, J.; Chan, H.; Kim, C. A Mussel Inspired Self-Expandable Tubular Hydrogel with Shape Memory under NIR for Potential Biomedical Applications. *J. Mater. Chem. B* **2017**, *5*, 5373−5379.

(23) Leng, J.; Wu, X.; Liu, Y. Infrared Light-Active Shape Memory Polymer Filled with Nanocarbon Particles. *J. Appl. Polym. Sci.* **2010**, *114*, 2455−2460.

(24) Lu, H.; Yao, Y.; Huang, W.; Leng, J.; Hui, D. Significantly Improving Infrared Light-Induced Shape Recovery Behavior of Shape Memory Polymeric Nanocomposite via a Synergistic Effect of Carbon Nanotube and Boron Nitride. *Compos Part B Eng.* **2014**, *62*, 256−261.

(25) Fang, L.; Chen, S.; Fang, T.; Fang, J.; Lu, C.; Xu, Z. Shape-Memory Polymer Composites Selectively Triggered by Near-Infrared Light of Two Certain Wavelengths and Their Applications at Macro−/Microscale. *Compos. Sci. Technol.* **2017**, *138*, 106−116.

(26) Zhang, H.; Xia, H.; Zhao, Y. Optically Triggered and Spatially Controllable Shape-Memory Polymer-Gold Nanoparticle Composite Materials. *J. Mater. Chem. C* **2011**, *22*, 845−849.

(27) Li, P.; Li, D.; Zhang, L.; Li, G.; Wang, E. Cationic Lipid Bilayer Coated Gold Nanoparticles-Mediated Transfection of Mammalian Cells. *Biomaterials* **2008**, *29*, 3617−3624.

(28) Wei, H.; Zhang, Q.; Yao, Y.; Liu, L.; Leng, J. Direct-Write Fabrication of 4D Active Shape-Changing Structures Based on a Shape Memory Polymer and Its Nanocomposite. *ACS Appl. Mater. Interfaces* **2016**, *9*, 876−883.

(29) Nguyen, N.; Barnes, H.; Bowland, C.; Meek, M.; Littrell, C.; Keum, K.; Naskar, K. A Path for Lignin Valorization via Additive Manufacturing of High-Performance Sustainable Composites with Enhanced 3D Printability. *Sci. Adv.* **2018**, *4*, No. eaat4967.

(30) Fina, F.; Goyanes, A.; Gaisford, S.; Basit, A. Selective Laser Sintering (SLS) 3D Printing of Medicines. *Int. J. Pharm.* **2017**, *529*, 285−293.

(31) Kuang, X.; Wu, J.; Chen, K.; Zhao, Z.; Ding, Z.; Hu, F.; Fang, D.; Qi, H. J. Grayscale Digital Light Processing 3D Printing for Highly Functionally Graded Materials. *Sci. Adv.* **2019**, *5*, No. eaav5790.

(32) Le Fer, G.; Becker, M. 4D Printing of Resorbable Complex Shape-Memory Poly(Propylene Fumarate) Star Scaffolds. *ACS Appl. Mater. Interfaces* **2020**, *12*, 22444−22452.

(33) Song, Z.; Ren, L.; Zhao, C.; Liu, H.; Ren, L. Biomimetic Non-Uniform, Dual-Stimuli Self-Morphing Enabled by Gradient 4D Printing. *ACS Appl. Mater. Interfaces* **2020**, *12*, 6351−6361.

(34) Zhang, Y.; Huang, L.; Song, H.; Ni, C.; Wu, J.; Zhao, Q.; Xie, T. 4D Printing of a Digital Shape Memory Polymer with Tunable High Performance. *ACS Appl. Mater. Interfaces* **2019**, *11*, 32408−32413.

(35) Peng, W.; Zhang, G.; Zhao, Q.; Xie, T. Autonomous Off-Equilibrium Morphing Pathways of a Supramolecular Shape-Memory Polymer. *Adv. Mater.* **2021**, *33*, 2102473.

(36) Peng, W.; Zhang, G.; Liu, J.; Nie, S.; Wu, Y.; Deng, S.; Fang, G.; Zhou, J.; Song, J.; Qian, J.; Pan, P.; Zhao, Q.; Xie, T. Light-Coded Digital Crystallinity Patterns Toward Bioinspired 4D Transformation of Shape-Memory Polymers. *Adv. Funct. Mater.* **2020**, *30*, 2000522.

(37) Zhang, B.; Li, H.; Cheng, J.; Ye, H.; Sakhaei, A.; Yuan, C.; Rao, P.; Zhang, Y.; Chen, Z.; Wang, R.; He, X.; Liu, J.; Xiao, R.; Qu, S.; Ge, Q. Mechanically Robust and UV-Curable Shape-Memory Polymers for Digital Light Processing Based 4D Printing. *Adv. Mater.* **2021**, *33*, 2101298.

(38) Chen, G.; Jin, B.; Zhao, Q.; Xie, T. A Photo-Driven Metallo-Supramolecular Stress-Free Reversible Shape Memory Polymer. *J. Mater. Chem. A* **2021**, *9*, 6827−6830.

(39) Henry, J.; Simonet, M.; Pandit, A.; Neuenschwander, P. Characterization of a Slowly Degrading Biodegradable Polyesterurethane for Tissue Engineering Scaffolds. *J. Biomed. Mater. Res. A* **2010**, *82A*, 669−679.

(40) Lin, H.; Chang, C.; Young, W. Experimental and Analytical Study on Filling of Nano Structures in Micro Injection Molding. *Int. Commun. Heat. Mass.* **2010**, *37*, 1477−1486.

🔲 Recommended by ACS

Soft, Stretchable, and Pneumatically Triggered Thermochromic Optical Filters with Embedded Phosphorescence

Yang Jin, Michael D. Dickey, *et al.*

MAY 11, 2020
ACS APPLIED MATERIALS & INTERFACES READ 🔗

Three-Dimensional Printing of Liquid Crystals with Thermal Sensing Capability via Multimaterial Vat Photopolymerization

Dylan Joralmon, Xiangjia Li, *et al.*

MARCH 24, 2022
ACS APPLIED POLYMER MATERIALS READ 🔗

New Coupling Agent Structures for Preparing Filler-Polymer Hybrid Materials Under Soft Irradiation Conditions

Houssein Nasrallah, Mohamad EL-Roz, *et al.*

JULY 19, 2022
MACROMOLECULES READ 🔗

Intelligent Surface with Multi-dimensional Information Enabled by a Dual Responsive Pattern with Fluorescence and Wrinkle

Luzhi Zhang, Xuesong Jiang, *et al.*

JULY 20, 2022
MACROMOLECULES READ 🔗

Get More Suggestions >